

Fast focus field calculations

Marcel Leutenegger^a, Matthias Geissbühler^a, Iwan Märki^a, Rainer A. Leitgeb^{b,a}, Theo Lasser^a

^a Laboratoire d'Optique Biomédicale, Ecole Polytechnique Fédérale de Lausanne, Lausanne, Switzerland;

^b Center of Biomedical Engineering and Physics, Medical University of Vienna, Vienna, Austria

ABSTRACT

We present a method for fast calculation of the electromagnetic field near the focus of an objective with a high numerical aperture (NA). Instead of direct integration, the vectorial Debye diffraction integral is evaluated with the fast Fourier transform for calculating the electromagnetic field in the entire focal region. We generalize this concept with the chirp z transform for obtaining a flexible sampling grid and an additional gain in computation speed. Under the conditions for the validity of the Debye integral representation, our method yields the amplitude, phase and polarization of the focus field for an arbitrary paraxial input field in the aperture of the objective. Our fast calculation method is particularly useful for engineering the point-spread function or for fast image deconvolution.

We present several case studies by calculating the focus fields of high NA oil immersion objectives for various amplitude, polarization and phase distributions of the input field. In addition, the calculation of an extended polychromatic focus field generated by a Bessel beam is presented. This extended focus field is of particular interest for Fourier domain optical coherence tomography because it preserves a lateral resolution of a few micrometers over an axial distance in the millimeter range.

Keywords: Focus fields, Debye diffraction integral, Fourier transform, chirp z transform.

Copyright: Copyright 2008 Society of Photo-Optical Instrumentation Engineers. This paper was published in Proceedings of SPIE 6861, 68610R (2008) and is made available as an electronic reprint with permission of SPIE. One print or electronic copy may be made for personal use only. Systematic or multiple reproduction, distribution to multiple locations via electronic or other means, duplication of any material in this paper for a fee or for commercial purposes, or modification of the content of the paper are prohibited.

1. INTRODUCTION

The plane wave spectrum (PWS) method is a well-known and efficient technique for calculating the propagation and diffraction of electromagnetic (EM) fields. Its efficiency lies in the ability to propagate EM fields from one plane to another using the fast Fourier transform (FFT). This concept is the essence of the Debye approximation and is often used for the calculation of the EM focus field.^{1,2} However, for focal field calculations in microscopy, in particular for optical systems with high numerical aperture (NA), this classical problem turns into a computational challenge due to the highly oscillatory behaviour of the involved functions. In addition, polarization effects cannot be neglected rendering the calculation long and tedious. Recent techniques in microscopy and tomography such as the extended focus field,³ microscopy beyond the Abbe resolution limit and point-spread function engineering as advanced by S. Hell and his group,⁴ or rigorous *ab initio* calculations for fluorescence fluctuation spectroscopy⁵ amplify the demand for fast focus field calculations.

In this paper we revisit the Debye approximation and propose a novel and flexible implementation of the Debye integral incorporating the effects of amplitude, phase and polarization in an overall manner. This new implementation is particularly suited for rapid numerical evaluation and requires substantially less effort for calculating the amplitude, phase and polarization of an EM field distribution generated by a high NA microscope objective. Section 2 introduces the Debye approximation (c.f. Leutenegger et al. for details⁶). Section 3 presents selected examples, firstly the calculation of a few focus fields obtained with a standard $100 \times 1.45\text{NA}$ oil immersion objective, and secondly, the calculation of an extended polychromatic focus field (Bessel beam).

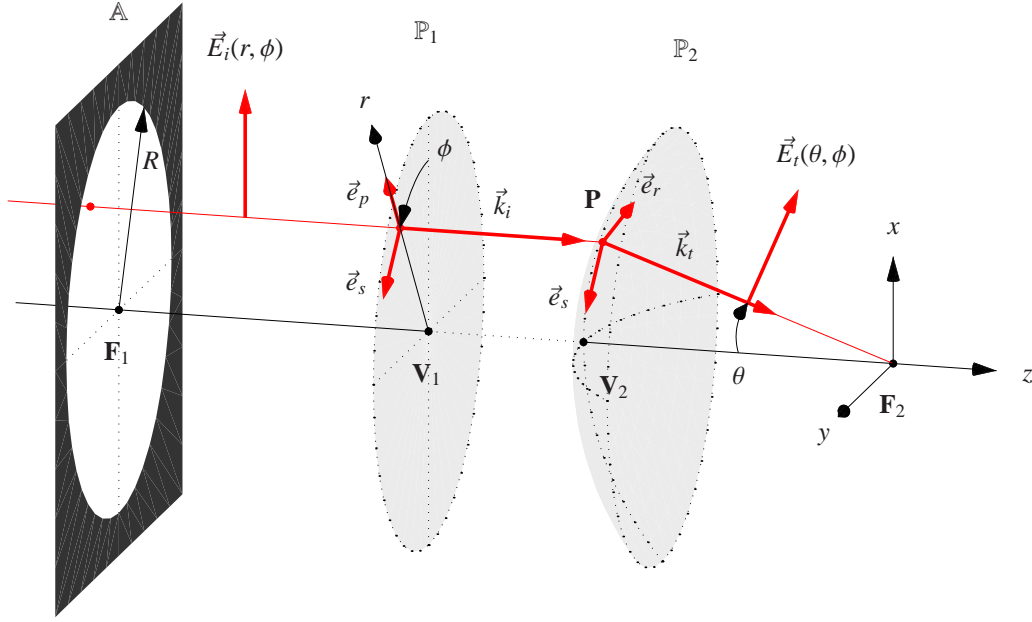


Figure 1. Optical setup. The objective is represented by the aperture stop \mathbb{A} with radius R , the principal planes \mathbb{P}_1 and \mathbb{P}_2 with vertex points \mathbf{V}_1 and \mathbf{V}_2 , and the foci \mathbf{F}_1 and \mathbf{F}_2 . The focal length f is given as $f = \overline{\mathbf{F}_1\mathbf{V}_1}$. The point \mathbf{P} is the intersection point of a ray with \mathbb{P}_2 and shows the relation of the position r at \mathbb{P}_1 of the incident wave \vec{E}_i to the propagation angle θ at \mathbb{P}_2 of the transmitted wave \vec{E}_t .

2. THEORY

This section establishes the basic formalism based on the Debye diffraction integral and the formulation of this integral as a Fourier transform.⁶ The basic optical layout and the respective coordinate systems are shown in Fig. 1. We assume that this imaging system obeys Abbe's sine condition, which is usually fulfilled for microscope objectives.

A coherent, monochromatic, paraxial wave field crosses the aperture stop \mathbb{A} , propagates towards the principal plane \mathbb{P}_1 and is transferred to the principal plane \mathbb{P}_2 . At \mathbb{P}_2 , the wave field is refracted and focused towards the focal point \mathbf{F}_2 . The point \mathbf{P} lies on the principal plane \mathbb{P}_2 and illustrates the focusing of a ray at \mathbb{P}_2 towards the focal point \mathbf{F}_2 . The spherical surface \mathbb{P}_2 is centered at \mathbf{F}_2 and the deflection angle θ at the position \mathbf{P} is given by

$$\sin \theta = \frac{r NA}{R n_t} \quad (1)$$

where r is the off-axis coordinate of the incident wave on \mathbb{P}_1 , R the aperture stop radius, NA the numerical aperture of the objective and n_t the index of refraction behind the \mathbb{P}_2 surface. Because the aperture \mathbb{A} is placed in the back focal plane, the imaging system is telecentric. Within our representation, the wave propagation from the aperture plane \mathbb{A} to the principal plane \mathbb{P}_1 can be calculated in most cases with classical Fourier optics principles.

For calculating the transmitted field $\vec{E}_t(\theta, \phi)$ at \mathbb{P}_2 , the incident field $\vec{E}_i(r, \phi)$ at \mathbb{P}_1 is typically decomposed into a radial (p-polarized) and a tangential component (s-polarized). Hence, the amplitude, phase and polarization of the transmitted field at \mathbb{P}_2 is

$$\vec{E}_t(\theta, \phi) = t_p(\vec{E}_i \cdot \vec{e}_p) \vec{e}_r + t_s(\vec{E}_i \cdot \vec{e}_s) \vec{e}_s \quad (2)$$

where $t_p(\theta, \phi)$ and $t_s(\theta, \phi)$ are the transmission coefficients and $\vec{e}_p(\theta, \phi)$, $\vec{e}_r(\theta, \phi)$ and $\vec{e}_s(\theta, \phi)$ the unit vectors for p- and s-polarization, respectively. Accumulated phase distortions (aberrations) at \mathbb{P}_2 as well as attenuations (apodization) caused by the objective are integrated in the complex transmission coefficients t_p and t_s . As we assume the incident field to be paraxial, the axial component E_{iz} is small against the lateral components $E_{ix,y}$ and can be neglected even if the incident phase is not constant. In the Debye approximation, the transmitted field \vec{E}_t is the *plane wave spectrum* of the focus field \vec{E}

Send correspondence to Marcel Leutenegger: marcel.leutenegger@a3.epfl.ch

near \mathbf{F}_2 . Therefore, the electric field \vec{E} at a point (x, y, z) near the focus \mathbf{F}_2 is obtained by integrating the propagated plane waves, that is

$$\vec{E}(x, y, z) = -\frac{if}{\lambda_0} \iint_{\Omega} \vec{E}_t(\theta, \phi) e^{i(k_z z - k_x x - k_y y)} d\Omega = -\frac{if}{\lambda_0} \int_0^{\Theta} \sin \theta \int_0^{2\pi} \vec{E}_t(\theta, \phi) e^{i(k_z z - k_x x - k_y y)} d\phi d\theta. \quad (3)$$

The phase factor $e^{ik_z z}$ accounts for the phase accumulation when propagating along the z -axis, whereas the term $e^{-i(k_x x + k_y y)}$ represents the phase difference of the wave front at off-axis points (x, y, z) with respect to the on-axis point $(0, 0, z)$. The integration extends over the solid angle Ω under which \mathbb{P}_2 is observed at \mathbf{F}_2 , i.e. $\sin \Theta = NA/n_t$. The wave vector \vec{k}_t is simply given by

$$\vec{k}_t(\theta, \phi) = k_0 n_t \begin{pmatrix} -\cos \phi \sin \theta \\ -\sin \phi \sin \theta \\ \cos \theta \end{pmatrix} \quad \text{where} \quad k_0 = \frac{2\pi}{\lambda_0}. \quad (4)$$

The evaluation of Eq. (3) is usually performed with a direct numerical integration taking into account the coordinate transformations, which results in the Richard-Wolf integral representation.^{7,8} Instead of the common ansatz, a (θ, ϕ) -sampling with constant $d\Omega = \sin \theta d\theta d\phi$ was introduced. Besides minimizing the number of sampling points along θ , the calculation of the integrand and its integration can be merged in a single matrix product resulting in a further reduction of the computation time. This evaluation of the Debye diffraction integral (3) is quite fast but still much slower than the conventional computation of a Fraunhofer diffraction integral. However, Eq. (3) can be easily rewritten as a Fourier transform by splitting the phase factor into a lateral and an axial term, and by performing the integration over \mathbb{P}_1 instead of \mathbb{P}_2 . Using Eq. (1) and (4), the integration step $d\Omega$ for a sampling over \mathbb{P}_2 is projected onto \mathbb{P}_1 , which yields

$$d\Omega = \left(\frac{NA}{Rn_t}\right)^2 \frac{r dr d\phi}{\cos \theta} = \left(\frac{NA}{Rn_t}\right)^2 \frac{dx dy}{\cos \theta} = \frac{1}{k_t^2} \frac{dk_x dk_y}{\cos \theta}. \quad (5)$$

Insertion of this sampling step into Eq. (3) results in

$$\vec{E}(x, y, z) = -\frac{if}{\lambda_0 k_t^2} \iint_{r < R} (\vec{E}_t(\theta, \phi) e^{ik_z z} / \cos \theta) e^{-i(k_x x + k_y y)} dk_x dk_y. \quad (6)$$

Extending now the integration over $(k_x, k_y) \in \mathbb{R}^2$ by setting $|\vec{E}_t| = 0$ for $r > R$ allows to rewrite the Debye diffraction integral as a Fourier transform of the weighted field \vec{E}_t , which finally results in

$$\vec{E}(x, y, z) = -\frac{if}{\lambda_0 k_t^2} \mathcal{F}_{x,y}(\vec{E}_t(\theta, \phi) e^{ik_z z} / \cos \theta). \quad (7)$$

This is the main result of this section. The Debye integral is now expressed as a two-dimensional Fourier transform $\mathcal{F}_{x,y}$ of the field distribution in the aperture \mathbb{A} projected on \mathbb{P}_2 , which can be evaluated with the fast Fourier transform (FFT) or the chirp z transform (CZT).⁶ The similarity of this expression with the conventional Fraunhofer diffraction integral is obvious. For a low NA imaging system, the weighting factor is approximated by $1/\cos \theta \approx 1$ and Eq. (7) is equivalent to the Fraunhofer diffraction integral.

3. APPLICATIONS

In this section, we present several case studies by calculating the focus fields achieved with a standard high NA oil immersion objective. The focus fields in the vicinity of the interface into the aqueous sample are presented for three cases: (1) a simple glass–water interface, (2) a glass-supported gold film–water interface and (3) a glass-supported silver film–water interface. Last but not least, the calculation of an extended polychromatic focus field generated by a Bessel beam is presented. This extended focus field is of particular interest for Fourier domain optical coherence tomography (FDOCT) because it preserves a lateral resolution of a few micrometers over an axial distance in the millimeter range.

3.1 Focus fields with oil immersion objectives

Current state of the art oil immersion objectives provide a very high lateral and axial resolution for imaging in the vicinity of a cover slide–sample interface. These objectives allow for instance total internal reflection excitation in the evanescent field penetrating only a fraction of a wavelength into the sample, which provides an outstanding axial confinement for highly surface-sensitive measurements. The following calculations outline the performance ideally achieved by a common oil immersion objective in case of confocal illumination. The calculations assume a $100\times 1.45\text{NA}$ oil immersion objective with an aperture diameter $\varnothing_{\text{A}} = 6\text{mm}$ and an x polarized laser beam with 633nm wavelength and a Gaussian e^{-2} beam waist of $w_{\text{A}} = 5\text{mm}$ at the aperture A .

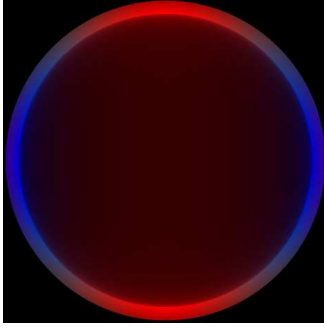


Figure 2. Transmitted field components $I_{xyz} \propto |E_{t,xyz}|^2$. The x component is shown in red, y in green and z in blue, respectively.

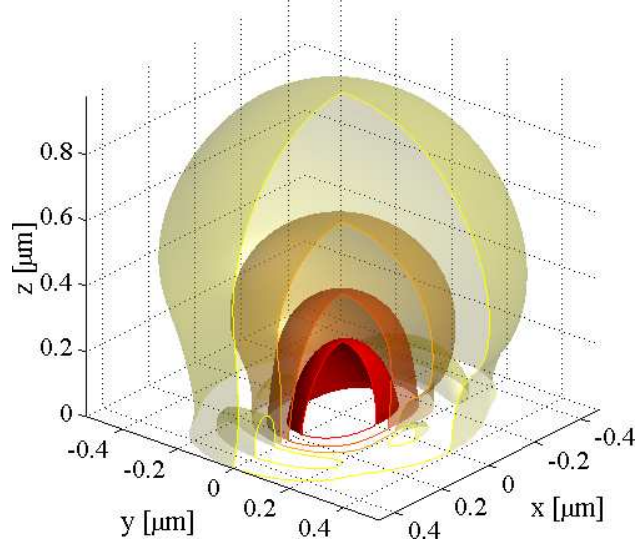


Figure 3. Focus field at the cover glass–water interface obtained with a $100\times 1.45\text{NA}$ oil immersion objective. The incident laser beam has a Gaussian e^{-2} waist of 5mm to overfill the objective aperture A of 6mm diameter. The laser beam is x polarized and has a wavelength of 633nm .

As a first example, the focus field at a cover glass–water interface is calculated. The intensity distribution of the transmitted field \vec{E}_t is shown in Fig. 2. At supercritical angles, i.e. for the outer aperture region where $\text{NA} > 1.33$, the evanescent field is easily identified by its characteristic intensity increase. As the incident polarization is linear along the x axis, the x component (red) is dominant except for a strong z component (blue) in the evanescent field. Figure 3 shows the corresponding focus field in the aqueous sample. The focus field is outlined with iso-intensity surfaces of $I = e^{-1...4} I_{\text{max}}$. In a confocal laser scanning microscope, a lateral resolution of $\Delta x \approx 220\text{nm}$ and $\Delta y \approx 180\text{nm}$ would be achieved.

As second example, the cover glass is covered with a 38nm thin gold film and the focus field at the gold–water interface is calculated. A relative dielectric constant $\epsilon_{\text{Au}} = -9.39 + 1.15i$ of gold is assumed. The film thickness of 38nm optimizes surface plasmon coupling near the aperture edge as shown in Fig. 4. Due to the dominant z polarization and the angular filtering by the plasmon coupling, the focus field in Fig. 5 shows a very particular profile similar to a tunnel along the y axis.

As third example, the cover glass is covered with a 55nm thin silver film and the focus field at the silver–water interface is calculated. A relative dielectric constant $\epsilon_{\text{Ag}} = -18.28 + 0.46i$ of silver is assumed. With a film thickness of 55nm , the optimal surface plasmon coupling occurs for an NA of 1.40 , which is well inside the aperture field shown in Fig. 6. Figure 7 shows the focus field, which inherits its rotational symmetry from the incident field with radial polarization. In the central peak, the z polarization is dominant whereas xy polarization prevails in the first side lobe. In comparison with the previous example, the plasmon coupling through the silver is much stronger than through gold because the optimal film thickness and the optimal incidence angle are both achievable with silver.

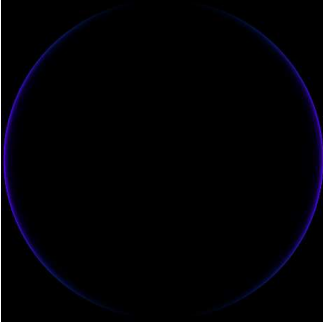


Figure 4. Transmitted field components (x red, y green, z blue).

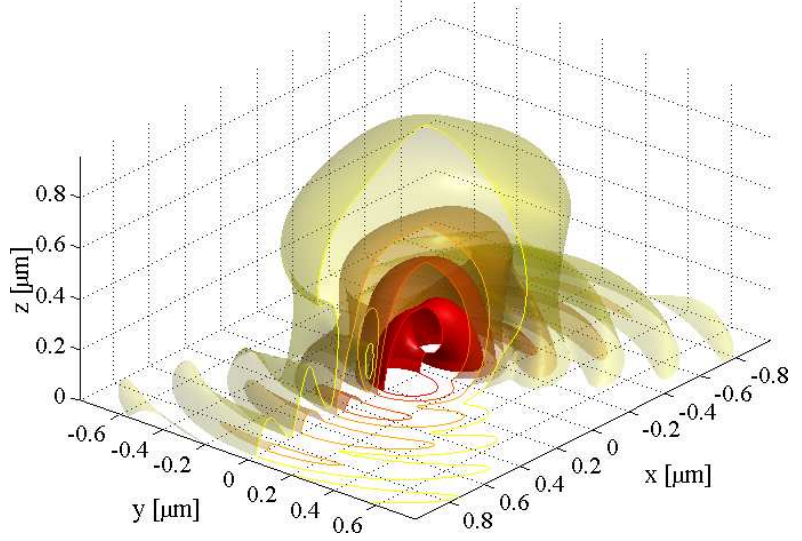


Figure 5. Focus field at the cover glass–38nm gold film–water interface obtained with a $100\times 1.45\text{NA}$ oil immersion objective.

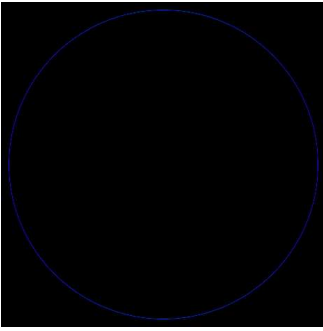


Figure 6. Transmitted field components (x red, y green, z blue).

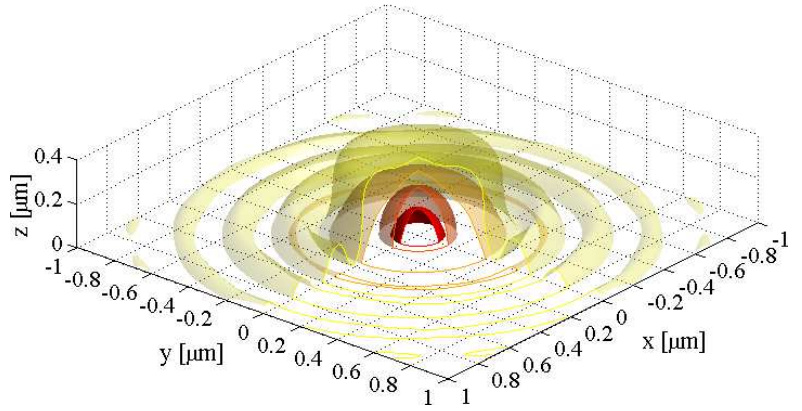


Figure 7. Focus field at the cover glass–55nm silver film–water interface obtained with a $100\times 1.45\text{NA}$ oil immersion objective and radial polarization of the incident field.

3.2 Extended depth of focus for Fourier domain optical coherence tomography

Optical coherence tomography (OCT) is a well-known, non-invasive, three-dimensional optical imaging method. Using a broadband light source, axial sectioning is achieved by interfering the back-reflected light from the sample with unaltered light from the reference arm of similar optical path length. In OCT, the axial resolution Δz is therefore (only) limited by the (detected) bandwidth $\Delta\lambda$ of the light source. As with conventional optical imaging, its lateral resolution Δr scales with λ_0/NA , where λ_0 is the free space wavelength and NA the numerical aperture of the imaging optics. Using a coherence gating in OCT, it is therefore possible to decouple axial and lateral resolution. In addition, due to the coherent amplification, OCT can achieve very high sensitivity for imaging the structure of transparent biological samples, i.e. small changes in refraction index already yield sufficient contrast for quantitative measurements.

Instead of a sequential depth scanning with the reference arm, Fourier domain OCT (FDOCT) simultaneously reads the full depth profile encoded in the measured interferogram spectrum.^{9,10} The sample structure is then obtained by Fourier-transforming these measured spectra. The main advantages of FDOCT are (a) a much faster acquisition as only lateral sample scanning is required,¹¹ (b) an improved phase stability due to fixed optical paths¹² and (c) an even better sensitivity (Fourier advantage). However, as the depth profile is recorded at once, a sharp image of lateral features is only obtained within the depth of focus (DOF). As the $\text{DOF} \propto \text{NA}^{-2}$ and $\Delta r \propto \text{NA}^{-1}$, enlarging the DOF usually means sacrificing lateral resolution. This limitation was overcome by using a Bessel beam for the sample illumination.¹³ The Bessel beam provides

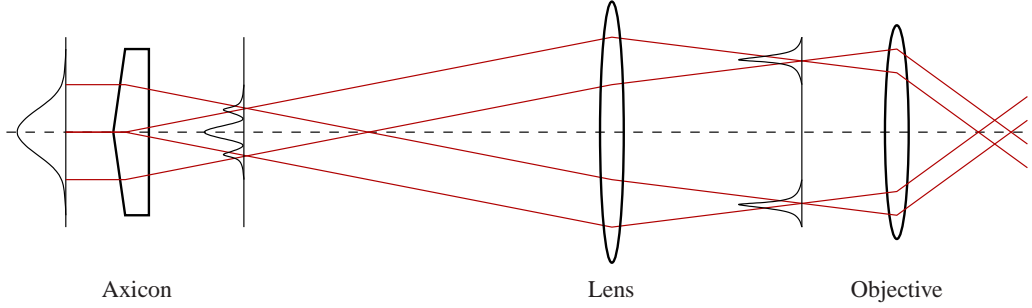


Figure 8. Sample illumination with a linear axicon and a telescope. The incident laser beam has a Gaussian waist of 3.4mm at $\lambda_0 = 785\text{nm}$ wavelength. The power spectrum of the fs-pulsed Ti:Sapphire laser is shown in Fig. 9. The linear axicon (20mm clear aperture, 178° full cone angle, BK7 glass) induces a converging conical wavefront. The lens ($f_l = 450\text{mm}$ focal distance, 22mm clear aperture) and the $10 \times 0.30\text{NA}$ objective ($f_o = 16.4\text{mm}$, $\varnothing_A = 10\text{mm}$ aperture) image the Bessel pattern into the sample with a $28\times$ demagnification.

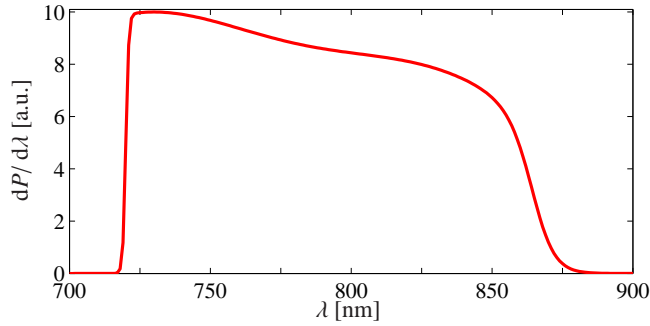


Figure 9. Ti:Sapphire spectrum transmitted into the sample. Central wavelength $\lambda_0 = 785\text{nm}$, bandwidth $\Delta\lambda \approx 140\text{nm}$.

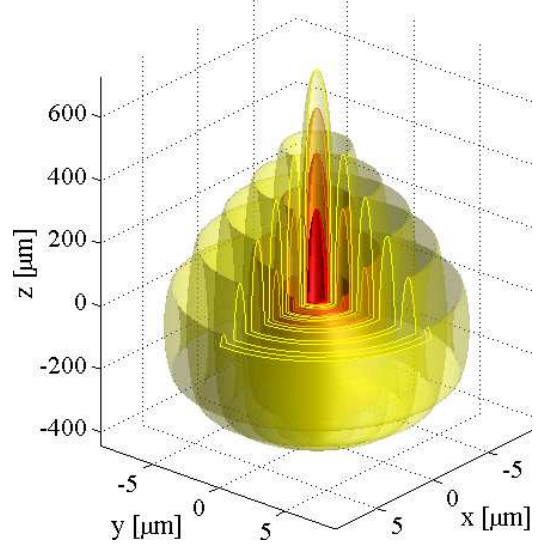


Figure 10. Illuminating Bessel beam for an extended DOF. Note the different scaling of the z axis.

a high lateral confinement (Δr in the order of λ_0) over a very long axial distance z , i.e. $\text{DOF} \gg \Delta r$. Figure 8 shows the optical setup for creating the Bessel beam. The collimated broadband laser beam with a Gaussian beam profile suffers a conical wavefront distortion by passing through a linear axicon. This converging conical beam creates the desired Bessel pattern in the overlap region behind the axicon. A telescope consisting of a lens and the microscope objective demagnify this Bessel pattern and image it into the sample. Figure 9 shows the spectrum of the illuminating Bessel beam. Figure 10 shows the calculated Bessel beam consisting of an incoherent superposition of focus fields for $\lambda \in [720\text{nm}, 870\text{nm}]$ with 1nm steps. The illuminating needle of $550\mu\text{m}$ FWHM length has a central spot diameter of $2\Delta r = 2.5\mu\text{m}$ only! Note also that the initial linear polarization of the laser beam is well conserved because of the moderate NA.

4. CONCLUSIONS

We showed a fast and accurate implementation of the vectorial Debye integral for calculating the focus field of high NA objectives for arbitrary amplitude, phase and polarization distributions of the input field. The numerical evaluation with the fast Fourier transform is very efficient and allows a high flexibility of the input field. With the general chirp z transform, we extended our calculations to low NA focus fields requesting a non-linear scaling as shown by Li and Hsu^{14,15} (c.f. Sec. 3.2 for example). For low NA, the method converges quite naturally to a focus field given by the Fraunhofer approximation. In addition, we used a generalized pupil function (apodization) of high NA objectives taking into account amplitude and polarization distributions. The pupil function incorporates the Fresnel transmission coefficients and can contain wave

front aberrations as induced by real objectives. Based on these Fresnel coefficients, it is straightforward to include wave propagation through stratified media as shown with example (2) and (3) in Sec. 3.1.

On a 2GHz Pentium 4 computer, the monochromatic focus fields of Sec. 3.1 were calculated in about a minute each ($203^2 \times 76 \approx 3.1 \cdot 10^6$ points). The extended polychromatic focus field of Sec. 3.2 with a 1nm wavelength sampling was calculated in about five hours ($150 \times 203^2 \times 131 \approx 810 \cdot 10^6$ points).

In summary, our method allows fast and accurate calculations of the focus field in the entire focal region, which opens the path to fast simulations for point spread function engineering and image deconvolution in three-dimensional light microscopy.

ACKNOWLEDGMENTS

We are grateful to Herbert Gross, Carl Zeiss Oberkochen for many valuable comments and discussions. The support of the Swiss National Science Foundation (SNSF) (contract number 200021-103333) is greatly acknowledged.

REFERENCES

1. P. Debye, "Das Verhalten von Lichtwellen in der Nähe eines Brennpunktes oder einer Brennlinie," *Ann. Phys.* **30**, pp. 755–776, 1909.
2. P. Török, P. Varga, "Electromagnetic diffraction of light focused through a stratified medium," *Appl. Opt.* **36**, pp. 2305–2312, 1997.
3. G. Mikula, A. Kolodziejczyk, M. Makowski, C. Prokopowicz, M. Sypek, "Diffractive elements for imaging with extended depth of focus," *Opt. Eng.* **44**, 058001, 2005.
4. N. Huse, A. Schönle, S. W. Hell, "Z-polarized confocal microscopy," *J. Biomed. Opt.* **6**, pp. 480–484, 2001.
5. J. Enderlein, I. Gregor, D. Patra, T. Dertinger, U. B. Kaupp, "Performance of Fluorescence Correlation Spectroscopy for Measuring Diffusion and Concentration," *Chem. PhysChem.* **6**, pp. 2324–2336, 2005.
6. M. Leutenegger, R. Rao, R. A. Leitgeb, T. Lasser, "Fast focus field calculations," *Opt. Express* **14**, pp. 11277–11291, 2006.
7. E. Wolf, "Electromagnetic diffraction in optical systems, I. An integral representation of the image field," *Proc. R. Soc. London Ser. A* **253**, pp. 349–357, 1959.
8. B. Richards and E. Wolf, "Electromagnetic diffraction in optical systems, II. Structure of the image field in an aplanatic system," *Proc. R. Soc. London Ser. A* **253**, pp. 358–379, 1959.
9. E. Götzinger, M. Pircher, R. A. Leitgeb, C. K. Hitzenberger, "High speed full range complex spectral domain optical coherence tomography," *Opt. Express* **13**, pp. 583–594, 2005.
10. B. Grajciar, M. Pircher, A. F. Fercher, R. A. Leitgeb, "Parallel Fourier domain optical coherence tomography for in vivo measurement of the human eye," *Opt. Express* **13**, pp. 1131–1137, 2005.
11. R. A. Leitgeb, C. K. Hitzenberger, A. F. Fercher, "Performance of Fourier domain vs. time domain optical coherence tomography," *Opt. Express* **11**, pp. 889–894, 2003.
12. A. H. Bachmann, R. Michaely, T. Lasser, R. A. Leitgeb, "Dual beam heterodyne Fourier domain optical coherence tomography," *Opt. Express* **15**, pp. 9254–9266, 2007.
13. R. A. Leitgeb, M. Villiger, A. H. Bachmann, L. Steinmann, T. Lasser, "Extended focus depth for Fourier domain optical coherence microscopy," *Opt. Lett.* **31**, pp. 2450–2452, 2006.
14. Y. Li, E. Wolf, "Three-dimensional intensity distribution near the focus in systems of different Fresnel numbers," *J. Opt. Soc. Am. A* **1**, pp. 801–808, 1984.
15. W. Hsu, R. Barakat, "Stratton-Chu vectorial diffraction of electromagnetic fields by apertures with application to small-Fresnel-number systems," *J. Opt. Soc. Am. A* **11**, pp. 623–629, 1994.